

## Probing the pairing symmetry of the iron pnictides with electronic Raman scattering

G. R. Boyd,<sup>1</sup> T. P. Devereaux,<sup>2,3</sup> P. J. Hirschfeld,<sup>1</sup> V. Mishra,<sup>1</sup> and D. J. Scalapino<sup>4</sup><sup>1</sup>Department of Physics, University of Florida, Gainesville, FL 32611, USA<sup>2</sup>Stanford Institute for Materials and Energy Sciences,

SLAC National Accelerator Laboratory, 2575 Sand Hill Road, Menlo Park, CA 94025

<sup>3</sup>Geballe Laboratory for Advanced Materials, Departments of Physics and Applied Physics, Stanford University, CA 94305.<sup>4</sup>Department of Physics, University of California, Santa Barbara, CA 93106-9530 USA

An important issue in the study of the iron-arsenic based superconductors is the symmetry of the superconducting gap, a problem complicated by multiple gaps on different Fermi surface sheets. Electronic Raman scattering is a flexible bulk probe which allows one in principle to determine gap magnitudes and test for gap nodes in different regions of the Brillouin zone by employing different photon polarization states. Here we calculate the clean Raman intensity for  $A_{1g}$ ,  $B_{1g}$  and  $B_{2g}$  polarizations, and discuss the peak structures and low-energy power laws which might be expected for several popular models of the superconducting gap in these systems.

PACS numbers:

## I. INTRODUCTION

Since their discovery<sup>1</sup>, there has been a considerable effort to understand the origin and nature of superconductivity in iron-pnictide materials (for early reviews see Refs. 2(4). Initial information on the structure of the gap is often provided by power laws in the temperature dependence of thermodynamic and transport properties, which are related to the topology of the superconducting gap in its nodal regions. Nuclear magnetic resonance (NMR) studies<sup>5(8</sup> showed a low temperature  $T^3$  spin lattice relaxation rate typical of a gap with nodes. However, penetration depth measurements<sup>9(15</sup> have been both to exponential activated  $T$ -dependence, indicative of a fully gapped state, and low- $T$  power laws. ARPES measurements on single crystals of 122-type materials<sup>16(21</sup> measured the spectral gap reporting isotropic or nearly isotropic gaps on all Fermi surface sheets. It is possible that these differences reflect genuinely different ground states in different materials. However, the complex interplay of multiband effects, unconventional pairing, and disorder leaves open the possibility that a single ground state symmetry exists in all the Fe-pnictides, and that differences in measured properties can be understood by accounting for electronic structure differences and disorder<sup>22,23</sup>. It is likely that a consensus will be reached only after careful measurements using various probes on the same material, and systematic disorder studies.

We argue here that measurement of the electronic Raman scattering in the superconducting state can provide important information on the structure of the bulk superconducting order parameter through its sensitivity to both symmetry and gap scales. Here we discuss the Raman scattering for some simple models of the Fe-pnictide superconductors. In general the energy of the peaks in the Raman intensity are directly related to the magnitude of the gaps on the various Fermi sheets. However, whether a given Raman polarization weights a given gap strongly or weakly depends on the polarization state of the measurement via the Raman vertex  $\chi_k$ . This is par-

ticularly important for superconductors where the gap is strongly momentum dependent, and was exploited successfully in cuprate materials to help determine the d-wave symmetry in those systems<sup>24(27</sup>. In addition, the presence of nodes and the dimensionality of the nodal manifold may be determined by comparison with low energy power laws in the Raman intensity in different polarization states.

In the Fe-pnictide materials, density functional theory calculations<sup>28,29</sup> for the paramagnetic state have generally found a multishheeted Fermi surface consisting of concentric, nearly circular hole pockets around the  $\Gamma$  point (here referred to as " $\Gamma$  sheets") and nearly circular electron pockets around the  $M$  points, or  $X$  point in the unfolded, 1-Fe zone (referred to as " $X$  sheets"). These sheets are plotted in Fig. 1. Spin fluctuation models of pairing<sup>30(33</sup> have usually found that the leading pairing instability had s-wave symmetry, and noted that the next leading channel had  $d_{x^2-y^2}$  symmetry. Wang et al.<sup>34</sup>, who studied the pairing problem using a functional renormalization group approach within a 5-orbital framework, also found that the leading pairing instability occurred in the s-wave channel, and that the next leading channel had  $d_{x^2-y^2}$  symmetry. These calculations differ according to whether or not actual nodes are found in the leading pairing states, but they all find large anisotropies over the Fermi surface sheets, not anticipated in the original predictions of extended-s-type states with isotropic gaps which changed sign between the  $\Gamma$  and  $X$  sheets<sup>35,36</sup>.

While ARPES experiments<sup>16(21</sup> have reported weakly anisotropic gaps, this may be due to momentum resolution issues and the difficulty of preparing good surfaces in these systems at present. In particular, the samples used in these experiments may be sufficiently dirty at the surface that considerable momentum averaging, with concomitant gap averaging, could be taking place<sup>23</sup>. Angle-dependent specific heat measurements in a magnetic field<sup>37</sup>, which probe the bulk, may be feasible in the future but are difficult at present due to the requirement of large clean crystals. Raman scattering with use

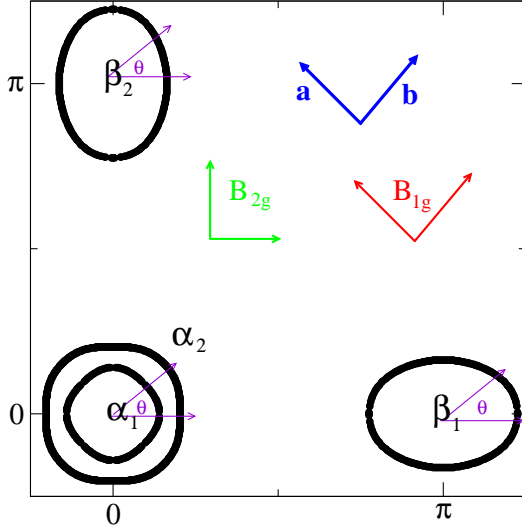


FIG. 1: Fermi surface of model Fe-pnictide represented in unfolded (1-Fe) Brillouin zone. The crystalline  $a, b$  axes are indicated in blue, and the polarization geometries for incoming and scattering photon polarizations are denoted for  $B_{1g}$  and  $B_{2g}$  geometries. Note that our symmetry notation is rotated by 45 degrees with respect to the lattice symmetries.

of different polarizations may therefore be the best current method of acquiring momentum-dependent information on the structure of the bulk superconducting order parameter. We discuss several cases below which should allow extraction of the crude momentum dependence and possible nodal structure of the order parameter over the Fermi surface. Some of these cases have been considered in an earlier paper by Chubukov et al.<sup>38</sup>, who however focussed solely on the  $A_{1g}$  polarization, and examined vertex corrections due to short-range interactions. However, they neglected "charge backflow" effect of the long-range part of the Coulomb interaction which is required to ensure charge conservation. Here we show that for the  $A_{1g}$  case, significant changes are to be expected due to the coupling of the  $A_{1g}$  Raman charge fluctuations due to the backflow effects.

While the expressions for the  $B_{1g}$  and  $B_{2g}$  channels are generally well-characterized by the bare bubble calculation for the cuprates, it is well-known that the  $A_{1g}$  contribution is significantly more complicated due to the issue of charge backflow as noted above, and to the number of different excitons which may be pulled down from a gap edge condensate. In system with several condensate pairing instabilities lying in close proximity in parameter space, strong excitonic peaks may occur. While the possibility of such excitonic modes is of interest for the pnictides, in this paper we focus on the generic quasi-particle features for Raman scattering, and will consider excitonic peaks in a future publication. Charge backflow and Coulomb screening is explicitly included in all  $A_{1g}$  calculations, but pair interaction corrections will be neglected. We will however also consider the possibility

that due to the form for the Raman vertices, which are allowed when there are multiple Fermi surfaces, there can also be backflow effects on symmetry channels other than  $A_{1g}$  in the Fe-pnictides.

We begin in Section II by considering model one-band clean systems with gaps inspired by proposals for the Fe-pnictides to illustrate what intuition we can gain regarding the Raman response for various polarizations. In Section III, we consider gaps on all four Fermi surfaces predicted by density functional theory. We present our conclusions in Section IV.

## II. ELECTRONIC RAMAN SCATTERING IN CLEAN SYSTEM

### A. General Theory

Raman scattering is the inelastic scattering of polarized light from a material. For a review see Ref. 24. The cross section of the scattered light is proportional to the imaginary part of the channel-dependent Raman susceptibility

$$\chi''(\omega) = \frac{1}{\omega} \text{Im} \left[ \sum_{\mathbf{q}} \chi(\mathbf{q}, \omega) \right] \sim \sum_{\mathbf{q}} \text{Im} \left[ \chi(\mathbf{q}, \omega) \right] \quad (1)$$

Here we will take a simple frequency independent form for the Raman vertices (non-resonant scattering) and write the effective Raman charge fluctuations in the  $\mathbf{q}$ -channel as

$$\chi(\mathbf{q}) = \sum_{n, m} \chi_{nm}(\mathbf{q}) c_n^y(\mathbf{q}) c_m(\mathbf{q}); \quad (2)$$

where  $n, m$  denote band indices.  $\chi_{nm}(\mathbf{q})$  denotes the momentum- and polarization-dependent Raman vertices, which may include intra- and interband transitions. Generally, the vertex is determined by both density and current matrix elements between the conduction band and the excited states, and has not been calculated for even simple metals like Al. However, the polarization geometries of the incoming and outgoing photons impose an overall symmetry due to the way in which excitations are created in directions determined by the electric field oscillations, and classifications of the anisotropy of the Raman vertices can be employed.

In this paper, in order to focus on general features for Raman scattering in the pnictides, we will neglect band structure features and treat all Fermi surface sheets as circles. This allows for a simple symmetry classifications for the Raman vertices as has been done in the cuprates. Expanding the polarization-dependent vertices in Fermi surface harmonics for cylindrical Fermi surfaces,

$$\begin{aligned} \chi_n(A_{1g}) &= a_n + b_n \cos(4\phi) \\ \chi_n(B_{1g}) &= c_n \cos(2\phi) \\ \chi_n(B_{2g}) &= d_n \sin(2\phi); \end{aligned} \quad (3)$$

with angle-independent band prefactors  $a_n; b_n; c_n; d_n$  setting the overall strength of the Raman amplitudes for band  $n$ . Since an isotropic density fluctuation vanishes for  $q \neq 0$ , it can be shown via Eq. 4 that the  $A_{1g}$  contribution  $a_n$  to the Raman vertex is cancelled by charge backflow and does not contribute to the scattering cross-section. This leaves the  $\cos(4\phi)$  as the first non-vanishing contribution in the expansion.

As shown in Fig. 1, we note that our choice of coordinates rests on the 1 Fe unit cell, which is rotated by 45 degrees with respect to the 2 Fe unit cell. Thus our symmetry notation is electronic and not associated with the lattice principal directions, and therefore our classifications are 45 degrees rotated with respect to conventional lattice classifications. Using lattice coordinates, what we call  $B_{1g}$  would be  $B_{2g}$ , and vice-versa. While this might create some confusion, it is convenient to understand the interplay of the angular dependence of the vertices and the energy gaps in the rotated 1 Fe unit cell frame, as shown in Fig. 1. This should be kept in mind however when one discusses, e.g., electronic excitations together with lattice excitations. Then our symmetry labels  $B_{1g}$  and  $B_{2g}$  would have to be interchanged.

Other forms for the Raman vertices are allowable, with the only requirement being that they must obey the transformation rules according to the relevant point group symmetries of the crystal. We note that for multi-sheeted Fermi surfaces shown in Fig. 1, there are different possible forms for the vertices other than Eq. 9. While the Raman vertices of the sheets must transform according to Eq. 9, for the sheets other forms for the vertices could be admissible. This includes, for the  $B_{1g}$  vertex for example, a vertex which is momentum independent on each sheet but of opposite sign. For the  $B_{2g}$  vertex, a Raman vertex which is p-wave like on each sheet (with a change of sign) would also be admissible. We will explore these possibilities in Sec. III.

For  $n$  bands crossing the Fermi level, the intraband Raman response in the absence of Coulomb screening and charge backflow is given by

$$\chi_{ij}^{scr}(\omega) = \frac{1}{N} \sum_{\mathbf{k}} \sum_n \chi_n(\mathbf{k})^2 \chi_n(\mathbf{k}; \omega); \quad (4)$$

where

$$\chi_n(\mathbf{k}; \omega) = \tanh \frac{E_n(\mathbf{k})}{2k_B T} \frac{4 \mathbf{j}_n(\mathbf{k}) \cdot \mathbf{j}_n(\mathbf{k})}{4E_n^2(\mathbf{k})} \frac{E_n(\mathbf{k})}{(\hbar\omega + i\gamma)} \quad (5)$$

is the Tsuneto function for the  $n^{\text{th}}$  band, having band dispersion  $\epsilon_n(\mathbf{k})$ , energy gap  $\Delta_n(\mathbf{k})$ , and quasiparticle energy  $E_n^2(\mathbf{k}) = \epsilon_n^2(\mathbf{k}) + \Delta_n^2(\mathbf{k})$ . Taking the imaginary part of Eq. (5) we then obtain for the Raman response at  $T = 0$

$$\text{Im} \chi_{ij}^{scr}(\omega) = \sum_n \text{Im} \chi_n^{ij}(\omega) = \sum_n \frac{N_{F,n}}{\omega} \text{Re} \left[ \frac{\mathbf{j}_n(\mathbf{k}) \cdot \mathbf{j}_n(\mathbf{k})}{\omega^2 - 4 \mathbf{j}_n(\mathbf{k}) \cdot \mathbf{j}_n(\mathbf{k})} \right]; \quad (6)$$

Since Raman scattering probes charge fluctuations in the long-wavelength limit, the role of the long-range Coulomb interaction is important. Isotropic charge fluctuations are coupled across all unit cells, and Raman scattering at low energies must vanish due to particle number conservation, leaving only an inelastic light scattering peak at the plasmon energy. Screening by the long-range Coulomb interaction can be taken into account by including couplings of the Raman charge density  $\tilde{\chi}$  to the isotropic density fluctuations and is given by

$$\tilde{\chi}_{ij}^{scr} = \tilde{\chi}_{ij} - \frac{\tilde{\chi}_i \tilde{\chi}_j}{\omega}; \quad (7)$$

with

$$\tilde{\chi}_i = \tilde{\chi}_j = \frac{1}{N} \sum_n \sum_{\mathbf{k}} \chi_n(\mathbf{k}) \chi_n(\mathbf{k}); \quad (8)$$

and

$$\tilde{\chi}_i = \frac{1}{N} \sum_n \sum_{\mathbf{k}} \chi_n(\mathbf{k}); \quad (9)$$

Eqs. (4-9) constitute closed form expressions for the intraband, non-resonant contribution to the Raman response.

It is clear that the Raman response is in general not simply additive with respect to the response calculated from each band separately. Incident photons can create anisotropic charge fluctuations according to the direction of the polarization light vector, and those charge fluctuations relax by emitting a scattered photon and redistributing charge density via intrinsic electron scattering mechanisms such as electron-impurity, electron-phonon, electron-electron interactions, or via breaking of Cooper pairs. The anisotropy of the charge fluctuations created with light can be controlled by aligning incident and scattered photon polarization vectors, transforming according to the elements of the irreducible point group of the crystal. For a material with  $D^{4h}$  tetragonal symmetry, and a single Fermi sheet, the  $B_{1g}$  and  $B_{2g}$  Raman responses are not coupled to the long-range Coulomb interaction. As a consequence, the Raman charge densities for these channels do not couple to the pure charge density channel, and the terms given in Eq. (8) vanish. However,  $A_{1g}$  fluctuations need not vanish over the unit cell, and therefore they can couple to isotropic charge density, giving the finite backflow represented by the second term in Eq. (7). We will see that this can also occur for the  $B_{1g}$  case for Raman vertices which are allowed when one has multiple Fermi surfaces as formed in the Fe-pnictides.

From the expression for the Raman response we see that in the case of an isotropic gap,  $\Delta_{\mathbf{k}} = \Delta$ , there should always be a peak at  $2\Delta$ . In an unconventional superconductor, depending on the polarization, this absorption peak is replaced by a peak or other structure at  $2\Delta_0$ , twice the maximum of the gap over the Fermi surface. The peak will be rounded by scattering, but still provides a measure of the magnitude of the gaps in

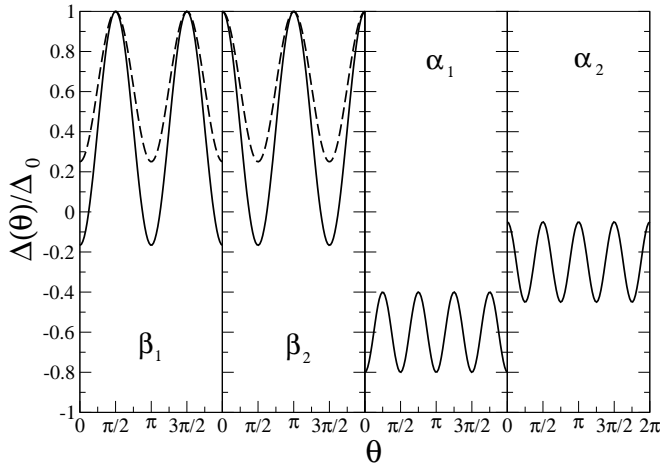


FIG. 2: The anisotropic energy gaps around the 4 Fermi surface sheets as a function of angle shown in Fig. 1. For the sheets, the solid line is for  $r = 1/4$  and the dotted line is for  $r = 0.6$  (see Eq. 14).

the system and may be compared to those determined from other experiments, e.g. ARPES and tunnelling. The  $B_{1g}$  and  $B_{2g}$  vertices in Eq. (3) have zeros in  $k$ -space and therefore weight the part of the Brillouin zone away from these zeros. This is observed, e.g. in the  $d$ -wave cuprates, where the sharp  $2\pi$  peak occurs in the  $B_{1g}$  channel only, while a less pronounced feature corresponding to a change in slope occurs at the same energy in the  $B_{2g}$  channel which weights the nodal regions most strongly. Furthermore, the existence of nodes in a gap creates low energy quasiparticles that cause a nonzero response for all frequencies. This is in sharp contrast to fully gapped superconductors whose response show a sharp gap edge with no low energy quasiparticles.

In what follows we consider separate cases of increasing complexity in order to display what features for Raman scattering in a multi-band system with different gap symmetries might be expected generically.

## B. Results for some special cases

### 1. Single Fermi sheet

In order to understand the type of behavior found for the multiband models of the Fe-pnictides, it is useful to begin with some special cases. Early on, motivated by the proximity of the Fe-pnictides to a  $(\pi, 0)$  spin density wave phase and the multiple Fermi surface structure found in LDA (local density approximation) calculations, a sign reversed  $s$ -wave gap was proposed.<sup>35</sup> It was suggested that spin-fluctuation scattering of electron pairs between the  $\alpha$  and  $\beta$  Fermi sheets could lead to pairing with an isotropic  $s$ -wave gap  $\Delta_0$  that changed sign between the  $\alpha$  and  $\beta$  Fermi surfaces. In this case, the Raman response would consist of a peak onset at  $2\Delta_0$  or several peaks

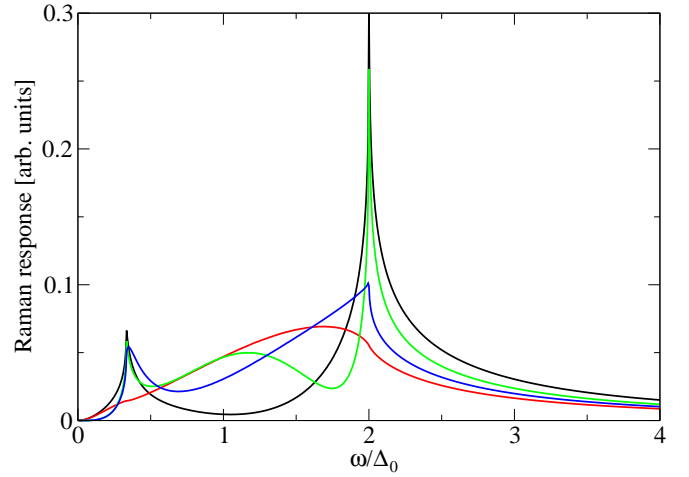


FIG. 3: The Raman response of the state with energy gap Eq. 10 for  $r = 1/4$ . Black/red lines denote  $B_{1g}=B_{2g}$ , and green/blue is the unscreened/screened  $A_{1g}$ , respectively. Note that our symmetry classifications are according to the geometry shown in Fig. 1. For lattice classifications,  $B_{1g}$  and  $B_{2g}$  should be interchanged.

if there were gaps of different magnitudes on the various Fermi surfaces. In the absence of impurity scattering and inelastic lifetime effects, this peak would vary as  $(\Delta_0)^{1/2}$  as  $\Delta_0$  approaches  $2\Delta_0$  from above.

Alternatively, RPA spin-fluctuation calculations and functional renormalization group studies find anisotropic  $s$ -wave gaps which can even have nodes on the Fermi surfaces as well as nearby  $d$ -wave gaps with nodes on the Fermi surfaces. Here, in order to examine the Raman signatures of such states, we consider the simple parameterization

$$\Delta(\theta) = \frac{\Delta_0}{1+r} (1 - r \cos(2\theta)) \quad (10)$$

This gap is plotted as a function of angle around a circular Fermi surface. Note, however, that for a single Fermi surface centered at  $(\pi, 0)$ , this state would not have four-fold symmetry. Instead, the Fermi surface parameterized by  $\theta$  is intended to represent a model for the  $\alpha_1$  sheet of the pnictides, and the Fermi surface angle is measured around  $(\pi, 0)$  rather than  $(0, 0)$ . When combined with the  $\beta_2$  sheet at  $(0, \pi)$ , the full  $s$ -wave symmetry of the state is restored. The gap in Eq. 10 is normalized such that  $\Delta_0$  is the maximum over the Fermi surface, and plotted for the values of  $r = r$  shown in Fig. 2. For  $r > 1$  the state has nodes on the Fermi surface, and for small values of  $r > 1$  these nodes move towards 0 and  $\pi$ . For  $r < 1$ , there are no nodes but for any nonzero  $r$  one has an anisotropic gap.

In Figs. 3 and 4 we exhibit the  $B_{1g}$ ;  $B_{2g}$ , unscreened  $A_{1g}$ , and screened  $A_{1g}$  Raman responses for the gaps given by Eq. (10), which are shown in the leftmost panel in Fig 2. In Fig. 3, where  $r = 1/4$ , there are gap nodes on the  $\beta$  sheets and one finds the expected

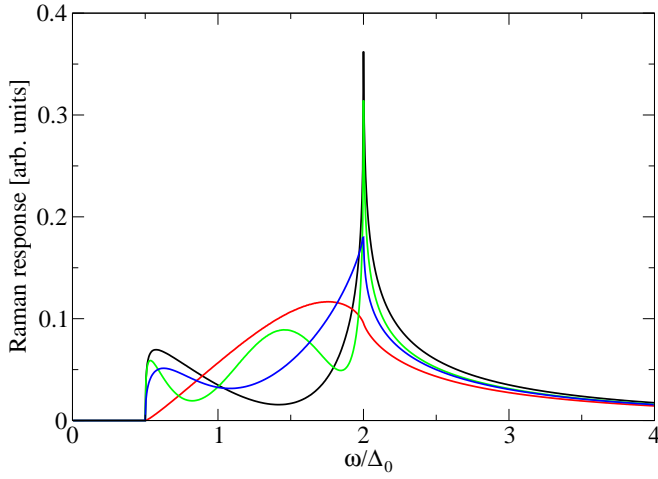


FIG. 4: The Raman response of the state with energy gap Eq. 10 for  $r = 0.6$ . Black/red lines denote  $B_{1g} = B_{2g}$ , respectively, green/blue is unscreened/screened  $A_{1g}$ .

low frequency power law behavior in which both response functions vary as  $\omega$ , following the low energy behavior of the density of states, since the nodes of the energy gap do not align with the nodes of the Raman vertices. For the gap edge  $\omega = 2\omega_{\max} = 2\omega_0$ , the  $B_{1g}$  and unscreened  $A_{1g}$  spectra have a  $\log |\omega - 2\omega_0|$  singularity. For the  $B_{2g}$  response, there is a change of slope at  $2\omega_0$  since the nodes of the vertex align with the gap maximum. A secondary  $\log$  singularity appears at  $\omega = 2\omega_{\min}$ , probed by the  $B_{1g}$  and  $A_{1g}$  vertices, but not  $B_{2g}$ . Screening, as pointed out before, removes all  $\log$  singularities from the unscreened  $A_{1g}$  response, leaving only a cusp-like behavior at  $\omega = 2\omega_{\min}/2\omega_{\max}$ .

For a nodeless anisotropic gap ( $r = 0.6$ ) shown as the dashed line in the  $\omega_1$  panel of Fig. 2, the Raman spectra are shown in Fig. 4. In this case, there is a gap in the low frequency spectra. Here, for  $r < 1$ ,  $\omega_{\min}$  occurs where the magnitude of the gap has a local minimum rather than a local maximum as it does for  $r > 1$ . This leads to a step discontinuity at  $\omega = \omega_0 = 0.5$  for the  $B_{1g}$  and  $A_{1g}$  spectra rather than the  $\log$  singularity seen in Fig. 3 for  $r = 1.6$ . The nodes of the Raman vertex for the  $B_{2g}$  response are aligned with  $\omega_{\min}$ , leading to a linear onset at  $\omega = 2\omega_{\min}$  rather than a step onset.

## 2. Two Fermi surface sheets

As indicated by Eq. 4, the  $A_{1g}$  Raman response for the case of a multi-sheet Fermi surface is not in general additive due to the Coulomb interactions and associated charge backflow. While no such backflow appears in the  $B_{1g}$  or  $B_{2g}$  channels for the present case, we will see in Sec. III that for Raman vertices which are allowed for the Fe-pnictides, there can be Coulomb backflow contributions to the  $B_{1g}$  channel. To illustrate this we calculate the  $A_{1g}$  Raman response for two Fermi surface sheets,

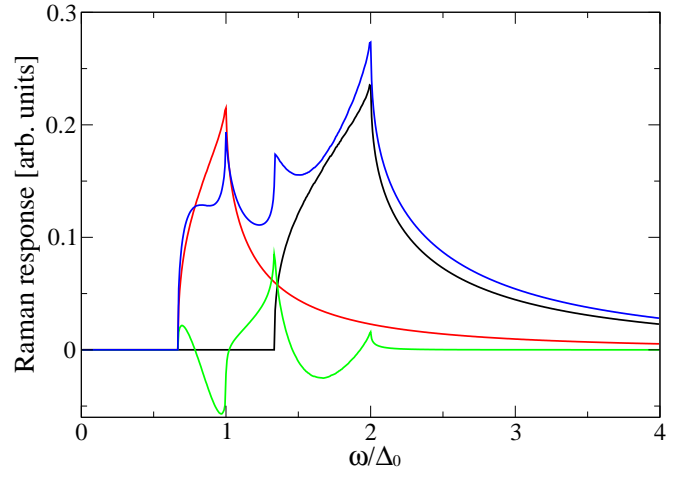


FIG. 5: The screened  $A_{1g}$  Raman response for 2 bands with  $\gamma_{1,2}(\mathbf{k})$  proportional to  $(1 + r \cos(4\phi)) = (1 + r)$  with  $r = 0.2$ , and the maximum gap on Fermi surface 1 equal to  $\omega_0$  and on Fermi surface 2 equal to  $\omega_0 = 2$ . (black = screened  $A_{1g}$  for band 1, red = screened  $A_{1g}$  for band 2, green = mixing term, blue = total response.)

where the energy gaps  $\gamma_{1,2}(\mathbf{k})$  are both proportional to  $(1 + r \cos(4\phi)) = (1 + r)$ , with  $r = 0.2$ . For simplicity, we take the gap maximum on one Fermi surface to be  $\omega_0$  and on the other  $\omega_0 = 2$ . We also take equal Raman vertices and density of states for each band.

Expanding Eqs. (4-9) for the case of 2 bands, the overall Raman response can be written as

$$\text{Im}_{sc}(\omega) = \text{Im}_1(\omega) + \text{Im}_2(\omega) + \text{Im}_{mix}(\omega); \quad (11)$$

where

$$\text{Im}_{1,2}(\omega) = \frac{1}{N} \sum_{\mathbf{k}} \gamma_{1,2}^2(\mathbf{k}) \gamma_{1,2}(\mathbf{k}; \omega) \frac{\sum_{\mathbf{k}'} \gamma_{1,2}(\mathbf{k}') \gamma_{1,2}(\mathbf{k}; \omega)^2}{N \sum_{\mathbf{k}'} \gamma_{1,2}^2(\mathbf{k}')} ; \quad (12)$$

and

$$\text{Im}_{mix}(\omega) = \frac{\sum_{\mathbf{k}} \gamma_1(\mathbf{k}; \omega) \sum_{\mathbf{k}'} \gamma_2(\mathbf{k}'; \omega)}{N \sum_{\mathbf{k}} (\gamma_1(\mathbf{k}; \omega) + \gamma_2(\mathbf{k}; \omega))} \frac{\sum_{\mathbf{k}} \gamma_1(\mathbf{k}) \gamma_1(\mathbf{k}; \omega)}{\sum_{\mathbf{k}} \gamma_1^2(\mathbf{k}; \omega)} \frac{\sum_{\mathbf{k}} \gamma_2(\mathbf{k}) \gamma_2(\mathbf{k}; \omega)}{\sum_{\mathbf{k}} \gamma_2^2(\mathbf{k}; \omega)} : (13)$$

Thus for  $A_{1g}$ , the screened Raman response can be considered as a sum of the screened response for each band, plus a mixing term. Here one can see that if the energy gaps and Raman vertices are the same for each band the mixing term vanishes, while for all other cases it is finite, reflecting the contribution from charge backflow. In this case, the light scattering induces interband charge transfer in order to recover particle number conservation when the charge fluctuations differ on the two bands.

As illustrated in Fig. 5, the screened  $A_{1g}$  Raman spectrum consists of contributions from each Fermi surface

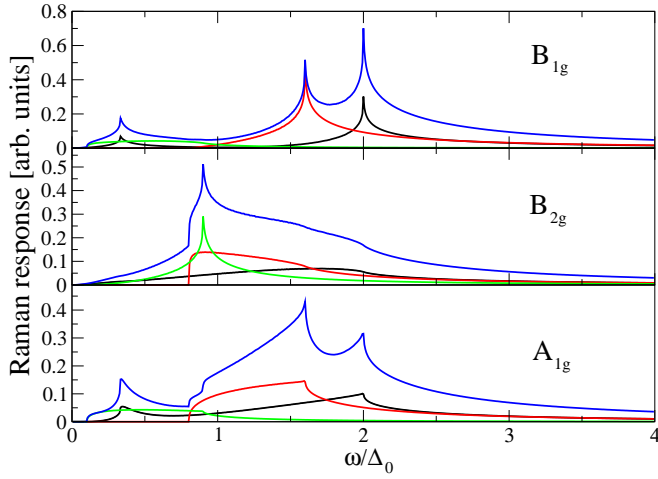


FIG. 6: The  $B_{1g}$ ,  $B_{2g}$  and screened  $A_{1g}$  Raman spectra for a four-sheeted Fermi surface, with  $r = 1.4$ . The black line corresponds to each contribution from the  $1,2$  bands, the red line to the  $1$  band, the green line  $2$ , and the blue line is the total response. Note that for the  $A_{1g}$  case (bottom panel) there is an interference term in addition to the sum of the contributions from each band. The energy gaps used are defined in the text.

with a gap scale differing by a factor of 2 and an interference contribution coming from the charge backflow. All singularities associated with the values of the gaps at the stationary points that would appear in the unscreened  $A_{1g}$  channel are removed and replaced by cusp-like behavior as in the single band case. However the structure of  $\chi_{sc}(\omega)$  is changed by the interference.

Interference terms also occur if the gaps are identical on each sheet but the Raman vertices differ. A more detailed examination of the role of charge backflow is presented in Ref. 27.

### III. THE FOUR FERMI SURFACE RAMAN SPECTRA

We would now like to extend this discussion of the features in the Raman intensity to the 4-Fermi surface model of the Fe-pnictides. Here we first consider the two sets of  $(\gamma)$  gap variations for the four Fermi surface sheets  $\gamma = 1, 2; 1$  and  $2$  shown in Fig. 4. Specifically, the energy gaps are taken to be (Fig. 2)

$$\begin{aligned} \gamma_{1,2} &= \frac{1}{2} \frac{1 - r \cos(2\gamma)}{1 + r}; \\ \gamma_1 &= 0.8 \frac{1 + \cos(4\gamma)}{2}; \\ \gamma_2 &= 0.4 \frac{1 - \cos(4\gamma)}{2}; \end{aligned} \quad (14)$$

As previously discussed, these gap choices are motivated by the anisotropic gaps found in RPA spin fluctuation and functional renormalization group calculations. The

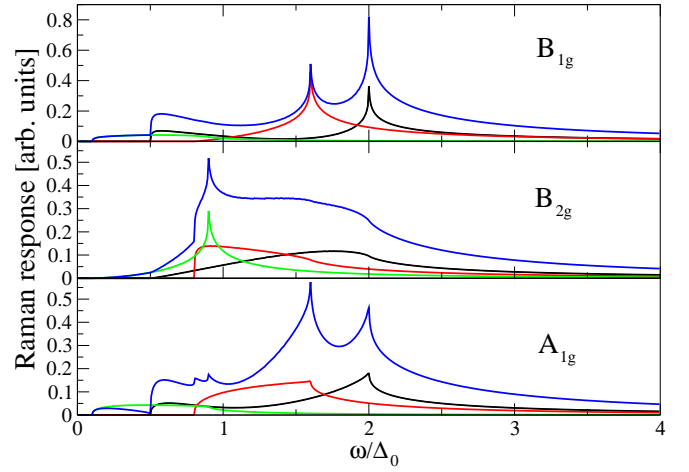


FIG. 7: Same as Fig. 6 but for  $r = 0.6$ .

amplitudes of the  $\gamma_1$  and  $\gamma_2$  gaps have been chosen to avoid an accidental overlap of singularities between the  $\gamma_1$  and  $\gamma_2$  gap extrema. The first of these, shown by the solid curves in Fig. 2, corresponds to an  $A_{1g}$  gap with nodes on the  $\gamma_1$  Fermi surfaces ( $r = 1.4$ ), and the second one is nodeless corresponding to the dashed curves ( $r = 0.6$ ). The  $B_{1g}$ ,  $B_{2g}$  and  $A_{1g}$  spectra for these two cases are shown in Figs. 6 and 7, respectively. The contribution from the individual Fermi surfaces are also indicated.

For the  $B_{1g}$  and  $B_{2g}$  spectra the structure seen in the total response are just the sum of the spectra from the individual Fermi surface sheets with the appropriate gaps shown in Fig. 2. For example, in Fig. 6, the  $B_{1g}$  response for the gap with nodes consists of a sum over different contributions coming from the two hole Fermi surfaces  $\gamma_1$  and  $\gamma_2$  and the sum of the spectra from the  $\gamma_1$  and  $\gamma_2$  electron Fermi surface sheets which are identical since Raman only probes  $j \parallel j$  and is not sensitive to the phase in the absence of impurities. Just as the for the previous discussion of the single Fermi surface case, one can easily identify the characteristic features coming from each Fermi surface shown in Fig. 6. The  $B_{1g}$  Raman response for a gap with nodes on the  $\gamma_1$  sheets (red curve) exhibits log singularities at  $\omega/\Delta_0$  equal to  $2j_{\gamma_1, \text{max}}/\Delta_0 = 0.15$  and  $2j_{\gamma_1, \text{min}}/\Delta_0 = 0.25$ . The  $\gamma_2$  sheet (green) contributes an additional log singularity at  $2j_{\gamma_2, \text{max}}/\Delta_0 = 0.16$ . Since the  $B_{1g}$  vertex has a node at the minimum value of the gap on the  $\gamma_1$  sheet the discontinuity at  $\omega/\Delta_0 = 0.8$  is eliminated leaving only a linear onset. The contribution of the  $\gamma_2$ -sheet has a similar linear onset at  $\omega/\Delta_0 = 0$  and a change in the slope at  $2j_{\gamma_2, \text{max}}/\Delta_0 = 0.8$  due to the fact that the  $B_{1g}$  Raman vertex has a node at the minimum and maximum values of the gap on the  $\gamma_2$  Fermi surface.

A similar discussion can be given for the  $B_{2g}$  case shown in the center panel of Fig. 6, where the total response is the sum of the contribution from the individual Fermi surface sheets with the  $B_{2g}$  Raman vertex. As discussed in the previous section, the screened  $A_{1g}$  response



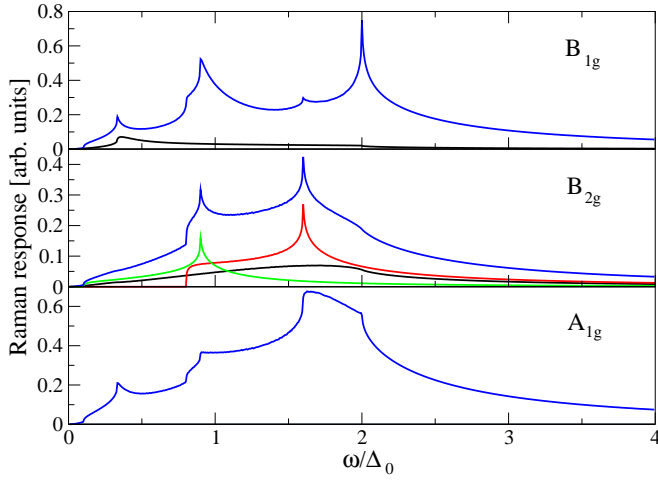


FIG. 8: Same as Fig. 6 but for different Raman vertices, given by Eq. (15).

shown in the lower panel of Fig. 6 contains the screened contributions from each band, plus an interference term with interference contributions coming from each pair of bands. All singularities are removed by the backflow, leaving the cusp-like behavior which can be tied to each of the gap extrema, as done for the other channels.

As mentioned in Sec. IIA, different forms for the Raman vertices are in principle allowable other than the ones given in Eq. (3), giving the Raman spectra shown in Figs. 6 and 7. Here we consider how different forms for the Raman vertices affect the general structure of the channel dependent Raman spectra. As an example, we consider the following form for the Raman vertices:

$$\begin{aligned}
 \chi_{1/2}(\mathbf{q})^{A_{1g}} &= 1 \\
 \chi_{1/2}(\mathbf{q})^{A_{2g}} &= 1; \\
 \chi_{1/2}(\mathbf{q})^{B_{1g}} &= \cos(2\mathbf{q} \cdot \mathbf{a}) \\
 \chi_{1/2}(\mathbf{q})^{B_{2g}} &= 1; \\
 \chi_{1/2}(\mathbf{q})^{B_{3g}} &= \sin(2\mathbf{q} \cdot \mathbf{a}) \\
 \chi_{1/2}(\mathbf{q})^{B_{4g}} &= \sin(\mathbf{q} \cdot \mathbf{a}): \quad (15)
 \end{aligned}$$

These vertices are all allowed by symmetry and have less anisotropy than the ones considered in Eq. 3 and thus highlight different gap structures. Moreover, due to the angle-independent form for the  $B_{1g}$  vertices on the sheets, screening must be included and the mixing terms are non-zero to give finite contributions to the spectra.

The resulting channel-dependent spectra are shown in Fig. 8 for the Fermi sheet gaps given in Eq. 14 with  $r = 1.4$ . For the  $B_{1g}$  case, Raman scattering from the individual sheets now is canceled by backflow due to the angular independent Raman vertices on those sheets, and two identical contributions arise from the sheets, as in Fig. 6. However, an additional mixing term arising from scattering interferences involving each separate sheet, gives a large contribution to the spectra, with peaks occurring at the energy scales given by the energy

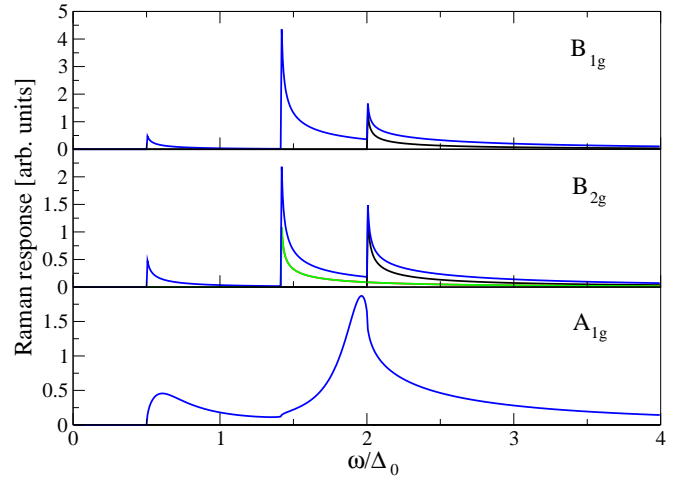


FIG. 9: Polarization dependence Raman response for the s state, having energy gaps given by Eq. (16) and Raman vertices given by Eq. (15). Color scales, denoting contributions from each band and the total response, are the same as in Figs. 6-8.

gap extrema on each sheet. For the  $B_{2g}$  spectra, the sinusoidal variation  $\sin(\mathbf{q} \cdot \mathbf{a})$  of the vertices on the sheets now allow for the highlighting of the gap maximum, giving a peak frequency at twice the gap maximum for the sheets, in contrast to the spectra shown in Fig. 6. A dramatic change of the spectra is observed for the  $A_{1g}$  channel. Due to backflow, the Raman response from each separate band vanishes identically for the constant vertices in Eq. (15), but due to the change in sign, the entire Raman spectra arises solely from the mixing terms. The positions of the cusp-like feature at  $\omega = 2\Delta_0$  are the same as that shown in Fig. 6 for a different form for the Raman vertices, however the overall spectra lineshape is qualitatively different. The overall structure of the lineshapes thus indicate that a proper account of the anisotropy of the Raman vertices may be needed in order to obtain a qualitative comparison with the experimental observed Raman spectra. This is a topic for further study.

Finally we consider a simple sign-changing s state on the four sheets:

$$\begin{aligned}
 \chi_{1/2}(\mathbf{q}) &= \frac{p}{2}; \\
 \chi_{1/2}(\mathbf{q}) &= 0; \quad \chi_{1/2}(\mathbf{q}) = 0; \quad \chi_{1/2}(\mathbf{q}) = 4; \quad (16)
 \end{aligned}$$

Using the vertices defined by Eq. 15, the resulting Raman spectra is shown in Fig. 9. Here, the square root divergence at twice the gap value is ubiquitous, displaying both in  $B_{1g}$  and in  $B_{2g}$ . The only polarization difference is that the contributions from the bands for the  $B_{1g}$  channel are screened, in contrast to the  $B_{2g}$  channel. Apart from this difference, the spectra are qualitatively similar, due to the mixing terms in  $B_{1g}$  which restore the singularity at  $\omega = 1.5\Delta_0$ . For the  $A_{1g}$  channel, the divergences are screened and the response maintains thresholds and peaks at twice the gap energy for each band.

## IV. CONCLUSIONS

Here we have studied the Raman scattering response for some simple models of the Fe-pnictide superconductors. Specifically, we considered two different anisotropic  $A_{1g}$  gaps, one with nodes and one without nodes, on four circular Fermi surfaces. Besides the well-known low frequency differences in the spectra for nodal and non-nodal gaps, we found a rich set of high frequency structures arising from stationary points of  $\chi''(\mathbf{q})$  on the various Fermi surfaces. Measurements of different polarizations may allow one to associate particular gap structures with individual Fermi surface sheets. If the gap has a large anisotropy as suggested by some calculations, there will be a rich Raman spectrum for different symmetry channels. However, if one has a relatively isotropic gap, such as the proposed sign-switched s wave, the spectrum should be simpler and sharper since for an isotropic gap the response has a square root singularity at  $2\phi_0$  rather than the weaker log singularity found for an anisotropic gap.

We have also discussed some of the unusual aspects of the Raman spectra to be anticipated in the Fe-pnictides due to their multisheeted Fermi surface electronic structure. In particular, Coulomb backscattering may affect the  $B_{1g}$  spectrum as well as  $A_{1g}$ . There are other unusual aspects, such as excitonic modes associated with short range interactions<sup>38</sup> or competing order parameter channels, which we have not explored here, but may make the spectra in these materials even richer. Work along these lines is in progress.

## Acknowledgments

We thank L. K. Emery, T. M. Aier, S. G. Raser for useful discussions. Research was partially supported by DOE DE-FG 02-05ER 46236 (PJH) and DOE DE-AC 02-76SF 00515 (TPD). DJS thanks the Stanford Institute of Theoretical Physics and the Stanford Institute for Materials and Energy Sciences for their hospitality.

- <sup>1</sup> Y. Kamihara, T. Watanabe, M. Hirano, and H. Hosono, *J. Am. Chem. Soc.* **130**, 3296 (2008).
- <sup>2</sup> M. V. Sadovskii, review talk on 90th anniversary of Physics Uspekhi arXiv:0812.0302.
- <sup>3</sup> H. Aoki, *Proc. Int. Conf. on Muon Spin Rotation, Relaxation and Resonance*, Tsukuba, Japan arXiv:0811.1656.
- <sup>4</sup> I. Mazin, J. Schmalian, arXiv:0901.4790.
- <sup>5</sup> R. Klingeler, N. Leps, I. Hellmann, A. Popa, C. Hess, A. Kondrat, J. Hamann-Borrero, G. Behr, V. Kataev, and B. Buechner, arXiv:0808.0708.
- <sup>6</sup> H.-J. Grafe, D. Paar, G. Lang, N. J. Curro, G. Behr, J. Wemer, J. Hamann-Borrero, C. Hess, N. Leps, R. Klingeler, and B. Buchner, *Phys. Rev. Lett.* **101**, 047003 (2008).
- <sup>7</sup> K. Ahilan, F. L. Ning, T. Imai, A. S. Sefat, R. Jin, M. A. McGuire, B. C. Sales, D. Mandrus, *Phys. Rev. B* **78**, 100501(R) (2008).
- <sup>8</sup> T. Y. Nakai et al., *J. Phys. Soc. Jpn.* **77**, 073701 (2008).
- <sup>9</sup> K. Hashimoto, T. Shibauchi, T. Kato, K. Ikada, R. Okazaki, H. Shishido, M. Ishikado, H. Kito, A. Iyo, H. Eisaki, S. Shamoto, and Y. Matsuda arXiv:0806.3149.
- <sup>10</sup> L. M. Malone, J. D. Fletcher, A. Serafini, A. Carrington, N. D. Zhigadlo, Z. Bukowski, S. Katrych, and J. Karpinski, arXiv:0807.0876.
- <sup>11</sup> C. Martin, R. T. Gordon, M. A. Tanatar, M. D. Vannette, M. E. Tillman, E. D. Mun, P. C. Canfield, V. G. Kogan, G. D. Samolyuk, J. Schmalian, and R. Prozorov, arXiv:0807.0876.
- <sup>12</sup> K. Hashimoto et al. arXiv:0810.3506.
- <sup>13</sup> R. T. Gordon, N. Ni, C. Martin, M. A. Tanatar, M. D. Vannette, H. Kim, G. Samolyuk, J. Schmalian, S. Nandi, A. Kreyssig, A. I. Goldman, J. Q. Yan, S. L. Bud'ko, P. C. Canfield, R. Prozorov, arXiv:0810.2295.
- <sup>14</sup> R. T. Gordon, C. Martin, H. Kim, N. Ni, M. A. Tanatar, J. Schmalian, I. I. Mazin, S. L. Bud'ko, P. C. Canfield, R. Prozorov, arXiv:0812.3683.
- <sup>15</sup> J. D. Fletcher, A. Serafini, L. Malone, J. Analytis, J.-H. Chu, A. S. Erickson, I. R. Fisher, A. Carrington, arXiv:0812.3858.
- <sup>16</sup> L. Zhao et al. *Chin. Phys. Lett.* **25**, 4402 (2008).
- <sup>17</sup> H. Ding, P. Richard, K. Nakayama, T. Sugawara, T. A. Rakane, Y. Sekiba, A. Takayama, S. Souma, T. Sato, T. Takahashi, Z. Wang, X. Dai, Z. Fang, G. F. Chen, J. L. Luo, N. L. Wang, *Europhys. Lett.* **83**, 47001 (2008).
- <sup>18</sup> T. Kondo, A. F. Santander-Syro, O. Copie, C. Liu, M. E. Tillman, E. D. Mun, J. Schmalian, S. L. Bud'ko, M. A. Tanatar, P. C. Canfield, A. Kaminski, *Phys. Rev. Lett.* **101**, 147003 (2008).
- <sup>19</sup> D. V. Evtushinsky, D. S. Inosov, V. B. Zabolotnyy, A. Koitzsch, M. Knupfer, B. Buchner, G. L. Sun, V. Hinkov, A. V. Boris, C. T. Lin, B. Keimer, A. Varykhalov, A. A. Kordyuk, S. V. Borisenko, arXiv:0809.4455.
- <sup>20</sup> K. Nakayama, T. Sato, P. Richard, Y.-M. Xu, Y. Sekiba, S. Souma, G. F. Chen, J. L. Luo, N. L. Wang, H. Ding, T. Takahashi, arXiv:0812.0663.
- <sup>21</sup> L. Wang, D. Qian, D. Hsieh, Y. Xia, L. Li, J. G. Checkelsky, A. Pasupathy, K. K. Gomes, C. V. Parker, A. V. Fedorov, G. F. Chen, J. L. Luo, A. Yazdani, N. P. Ong, N. L. Wang, M. Z. Hasan, arXiv:0812.2061.
- <sup>22</sup> A. B. Vorontsov, M. G. Vavilov, and A. V. Chubukov, arXiv:0901.0719.
- <sup>23</sup> V. Mishra, G. Boyd, S. G. Raser, T. M. Aier, P. J. Hirschfeld, D. J. Scalapino, submitted to PRB, arXiv:0901.2653.
- <sup>24</sup> T. P. Devereaux, R. Hackl, *Rev. Mod. Phys.* **79**, 175 (2007).
- <sup>25</sup> T. P. Devereaux, A. Kampf, *Int. J. Mod. Phys. B* **11**, 2093 (1995).
- <sup>26</sup> T. P. Devereaux, D. Einzel, *Phys. Rev. B* **51**, 16336 (1995).
- <sup>27</sup> T. P. Devereaux, A. V. Iosztek, and A. Zawadowski, *Phys. Rev. B* **54**, 12523 (1996).
- <sup>28</sup> D. J. Singh and M. H. Du, *Phys. Rev. Lett.* **100**, 237003 (2008).
- <sup>29</sup> C. Cao, P. J. Hirschfeld, H.-P. Cheng, *Phys. Rev. B* **77**,



- 220506(R) (2008).
- <sup>30</sup> K. Kuroki, S. Onari, R. Arita, H. Utsui, Y. Tanaka, H. Kontani and H. Aoki, Phys. Rev. Lett. 101, 087004 (2008).
  - <sup>31</sup> H. Ikeda, arXiv:0810.1828
  - <sup>32</sup> Y. Yanagi, Y. Yamakawa and Y. Ono, arXiv:0808.1192, 0809.3189
  - <sup>33</sup> S. Graser, T. A. Maier, P. J. Hirschfeld and D. J. Scalapino, arXiv:0812.0343.
  - <sup>34</sup> F. Wang, H. Zhai, Y. Ran, A. Vishwanath and D. H. Lee, arXiv:0807.
  - <sup>35</sup> I. I. Mazin, D. J. Singh, M. D. Johannes, and M. H. Du, Phys. Rev. Lett. 101, 057003 (2008).
  - <sup>36</sup> A. V. Chubukov, D. Efremov, and I. Eremin, Phys. Rev. B 78, 134512 (2008).
  - <sup>37</sup> S. Graser, G. R. Boyd, C. Cao, H.-P. Cheng, P. J. Hirschfeld, and D. J. Scalapino, Phys. Rev. B 77, 180514 (2008).
  - <sup>38</sup> A. V. Chubukov, I. Eremin, M. M. Korshunov, arXiv:0901.2102.